

Anisotropy of Low Energy Direct Photons in Relativistic Heavy Ion Collisions

T. Koide and T. Kodama

Instituto de Física, Universidade Federal do Rio de Janeiro, C.P. 68528, 21941-972, Rio de Janeiro, Brazil

We investigate the behavior of low energy photons radiated by the deceleration processes of two colliding nuclei in relativistic heavy ion collisions using the Wigner function approach for electromagnetic radiation fields. The angular distribution reveals the information of the initial geometric configurations. Such a property is reflected in the anisotropic parameter v_2 , showing an increasing v_2 as energy decreases, which is a behavior qualitatively different from v_2 from hadrons produced in the collisions.

I. INTRODUCTION

In the physics of relativistic heavy ion collisions, the determination of the initial collision geometry is one of the fundamental pieces to investigate the dynamics of the created matter such as quark-gluon plasma. Then the information of the reaction plane is indispensable to study the anisotropic collective flows of the matter. Such a geometry is deduced indirectly from, for example, the statistical average over an event ensemble by calculating the cumulant of the correlation functions of hadrons which are generated through very complex strong interactions [1]. On the other hand, photons do not suffer from strong interactions, and the so-called direct photons are considered to carry the information of the early stage of the collisions. Numerous works in this line have been done from the early days of the relativistic heavy ion program [2–18]. See Ref. [19] for a recent review on this subject and references therein.

Among various mechanisms for producing the direct photons, we can consider bremsstrahlung radiations. This process is usually modeled as classical radiations from the decelerated protons of the incident nuclei [2–11]. In Ref. [20], the authors focused on the behavior of the higher energy ($\gtrsim 1$ GeV) of the photons which are dominantly produced by the incoherent sum of the bremsstrahlung radiations from individual decelerated protons, reproducing the spectrum of the observed one [21]. In this case, any meaningful information for the initial geometry of the nuclear scale is expected to be washed out.

On the other hand, for the lower energies, electromagnetic fields may be generated *coherently* from each decelerating proton, when their spatial separation is the order of the corresponding wavelength of the radiations. If this occurs, we expect the following two effects. One is that the amount of the radiations increases as $\sim Z_{eff}^2$, instead of $2Z_{eff}$ in the incoherent case, where Z_{eff} is the effective number of the charges which contribute to the electromagnetic radiations in the collisions. The other is that the angular distribution of the radiated photons will reflect the geometric configuration due to the interference of radiations from the two incident nuclei. When we have a sufficient yield of the coherent photons in the very low transverse momentum p_T region, the elliptic flow v_2 for the direct photons will be dominated by such coherent

photons.

In this work, we study the photon spectrum and its angular distributions of the low energy photons, which are produced by the coherent radiations from two decelerated incident nuclei. We first calculate the electromagnetic fields by introducing the simplified trajectories of the two incident nuclei. These nuclei are treated as point-like objects with an effective charge Z_{eff} . From this, we obtain the phase space distribution of the photons with the help of the Wigner function which expresses the photon spectrum and the angular distribution. We further show that the corresponding anisotropic parameter v_2 reveals a very enhanced nature in the lower p_T .

In the following, we use $\hbar = c = \varepsilon_0 = \mu_0 = 1$ and the fine structure constant is defined by $\alpha_{EM} = e^2/(4\pi)$ in the SI (rationalized) unit.

II. MODEL OF COLLISIONS AND ELECTROMAGNETIC RADIATIONS

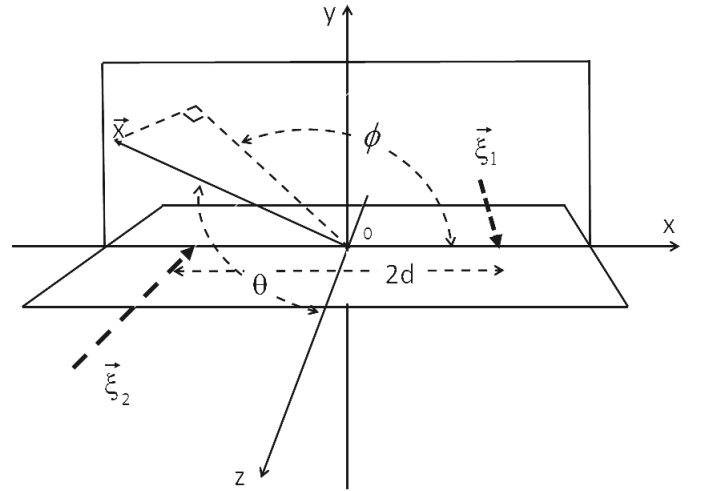


FIG. 1: The schematic figure for the collision of two incident nuclei.

Let us consider a collision of two identical nuclei with the impact parameter b . In the strong coherence limit, we can simplify the situation by replacing these nuclei with

point-like particles which have an effective charge Z_{eff} . One may expect that Z_{eff} is the same as the number of participant protons $Z_{part}(b)$ from one of nuclei, but more generally, only a portion of the participant protons can contribute to the coherent radiations. Then we have the restriction, $Z_{eff} \lesssim Z_{part}(b)$. We further consider that the protons in each nucleus will be completely stopped by the collisions with other protons or neutrons, as is the initial condition of the Landau hydrodynamic model. Our geometrical coordinate is represented in Fig. 1, where the z -axis is chosen as the collision direction and the two incident nuclei collide at $t = 0$.

In general, the deceleration by the collisions occurs in a finite time period, which is characterized by stopping time τ_S . For the ultra-relativistic heavy ion collisions, τ_S is given by the order of the Lorentz contracted thickness of the projectile, $\tau_S \sim R/\gamma$, where R and γ are the nuclear radius and the Lorentz factor, respectively. For relativistic limit $\gamma \gg 1$, then the stopping time will be very small. For the sake of simplicity, we consider the infinitesimal limit of τ_S . In this case, the deceleration is given by the Dirac delta function in time. See also the discussion in Appendix A.

Then the trajectories of the nuclei 1 and 2 are, respectively, expressed in the Cartesian coordinates as

$$\vec{\xi}_1(t) = \begin{pmatrix} d \\ 0 \\ t V_0 \theta(-t) \end{pmatrix}, \quad \vec{\xi}_2(t) = \begin{pmatrix} -d \\ 0 \\ -t V_0 \theta(-t) \end{pmatrix}, \quad (1)$$

where $2d$ represents the transverse distance between the two centers of mass of the respective participant protons (See Fig. 1). This is usually smaller than the impact parameter, $2d \lesssim b$. At infinite distance ($t = -\infty$), the nuclei move with a constant speed V_0 which should be less than one.

The solution of the Maxwell equations for these trajectories is given by the Liénard-Wiechert potential [22]. Since we are interested in the behaviors of the radiations at the detector position, we drop irrelevant contributions at infinite distance. Then, the contributions from the charge $\vec{\xi}_1(t)$ are given by

$$\begin{aligned} \vec{E}_1(\vec{x}, t) &= \frac{eV_0 Z_{eff}}{4\pi} \frac{1}{|\vec{x} - \vec{\xi}_1(t_1)|} \frac{1}{1 - \vec{\beta}_1 \cdot \vec{n}_1} \\ &\times \left\{ (1 - \vec{n}_1 \vec{n}_1^T) \vec{e}_z \right\} \delta(t_1), \\ \vec{B}_1(\vec{x}, t) &= \vec{n}_1 \times \vec{E}_1(\vec{x}, t). \end{aligned}$$

where \vec{e}_z is a unit vector of the z -axis and

$$\vec{n}_1 \equiv \frac{\vec{x} - \vec{\xi}_1(t_1)}{|\vec{x} - \vec{\xi}_1(t_1)|}, \quad \vec{\beta}_1 \equiv \frac{d\vec{\xi}_1}{dt} \bigg|_{t=t_1}$$

All these quantities appearing on the right hand sides are evaluated at the emission time t_1 , defined by the causality equation, $|\vec{x} - \vec{\xi}_1(t_1)| = t - t_1$.

Therefore, eliminating the emission times, $\vec{E}_1(\vec{x}, t)$ and $\vec{B}_1(\vec{x}, t)$ are reexpressed as

$$\vec{E}_1(\vec{x}, t) = \frac{eV_0 Z_{eff}}{4\pi} \frac{1}{r_-^3} \begin{pmatrix} -(x-d)z \\ -yz \\ (x-d)^2 + y^2 \end{pmatrix} \delta(t - r_-), \quad (2a)$$

$$\vec{B}_1(\vec{x}, t) = \frac{eV_0 Z_{eff}}{4\pi} \frac{1}{r_-^2} \begin{pmatrix} y \\ -(x-d) \\ 0 \end{pmatrix} \delta(t - r_-), \quad (2b)$$

where $r_- = \sqrt{(x-d)^2 + y^2 + z^2}$. The corresponding electromagnetic fields from $\vec{\xi}_2(t)$ can be obtained by replacing the two parameters, (d, V_0) by $(-d, -V_0)$ in Eq. (2).

III. WIGNER FUNCTION OF ELECTROMAGNETIC FIELDS

To extract the spectrum of the photons radiated from the classical electromagnetic fields, Ref. [20] employs an interpretation that the frequency distribution of the radiation energy as the energy distribution of photons with the help of Einstein's relation. On the other hand, it is known that the classical electromagnetic field can be interpreted as the wave function of the corresponding photons [23–26]. Here we employ this approach to calculate the photon angular distribution.

Let us introduce a complex vector function as

$$\vec{F} = \sqrt{\frac{1}{2}} (\vec{E} + i\vec{B}). \quad (3)$$

Then source-free Maxwell's equations can be reexpressed in a similar form to the Dirac equation as

$$i\partial_t \vec{F} = -i(\vec{T} \cdot \nabla) \vec{F}, \quad (4)$$

with a constraint,

$$\nabla \cdot \vec{F} = 0, \quad (5)$$

where \vec{T} is the spin-1 generator of $O(3)$. Equation (5) constrains only the initial condition of \vec{F} . From the definition, one can easily see that the energy density and the Poynting vector are expressed as $\vec{F}^* \cdot \vec{F}$ and $-i \vec{F}^* \times \vec{F}$, respectively. Other properties of this quantum mechanical interpretation of the vector wave function, see Ref. [25].

To discuss physical observables measured by a detector at a given location, it is convenient to introduce the phase-space distribution function, known as Wigner function. In the present case, we have

$$\begin{aligned} f_W(\vec{x}, \vec{p}, t) &\equiv \int d^3\vec{q} \vec{F}^*(\vec{x} + \vec{q}/2, t) \cdot \vec{F}(\vec{x} - \vec{q}/2, t) e^{i\vec{q} \cdot \vec{p}} \\ &= f_W^{(E)}(\vec{x}, \vec{p}, t) + f_W^{(B)}(\vec{x}, \vec{p}, t). \end{aligned}$$

where $f_W^{(E,B)}$ represents the contribution from the electric (magnetic) field. After some algebra, we find

$$f_W^{(E,B)}(\vec{x}, \vec{p}; t) = G^{(E,B)}(\vec{x} - \vec{d}, \vec{p}; t) + G^{(E,B)}(\vec{x} + \vec{d}, \vec{p}; t) - 2 \cos(2\vec{p} \cdot \vec{d}) G^{(E,B)}(\vec{x}, \vec{p}; t), \quad (6)$$

$$G^{(E,B)}(\vec{x}, \vec{p}; t) \equiv \int d^3 \vec{q} \times \left\{ \vec{F}^{(E,B)}(\vec{x} + \vec{q}/2, t) \cdot \vec{F}^{(E,B)}(\vec{x} - \vec{q}/2, t) \right\} e^{i\vec{q} \cdot \vec{p}}, \quad (7)$$

and

$$\vec{F}^{(E)}(\vec{x}, t) \equiv \sqrt{\frac{1}{2}} \frac{eV_0 Z_{eff}}{4\pi} \frac{1}{r^3} \begin{pmatrix} -xz \\ -yz \\ x^2 + y^2 \end{pmatrix} \delta(t - r),$$

$$\vec{F}^{(B)}(\vec{x}, t) \equiv \sqrt{\frac{1}{2}} \frac{eV_0 Z_{eff}}{4\pi} \frac{1}{r^2} \begin{pmatrix} y \\ -x \\ 0 \end{pmatrix} \delta(t - r).$$

Here, $r = |\vec{x}|$.

As is well-known, the Wigner function does not correspond to the phase-space distribution, since, in general cases, it can take negative values. However, as shown below, the large distance behavior guarantees the non-negativity of the Wigner function. Since \vec{x} and t are macroscopic quantities associated with the physical measurements by a detector, they are much larger than the magnitude of $1/p$, where p being the order of $\text{MeV} \sim \text{GeV}$. Thus, the significant contributions in the q integrals in Eq.(7) come from the domain satisfying $q \ll r$, t due to the exponential factor in the integrands. Therefore we can safely expand them with respect to q/r . The integrands contain the product of two delta functions with respect to t , which is approximately reexpressed as $\delta(t - \sqrt{(\vec{x} + \vec{q}/2)^2}) \delta(t - \sqrt{(\vec{x} - \vec{q}/2)^2}) \simeq \delta(t - r) \delta(q_{//})$, where $q_{//}$ is the component of \vec{q} parallel to \vec{x} . Then we have

$$G^{(E)}(\vec{x}, \vec{p}; t) = C(\vec{x}) \delta(t - r) \int d^2 \mathbf{q}_\perp e^{i\mathbf{p}_\perp \cdot \mathbf{q}_\perp} + O\left(\frac{1}{r^3}\right) \simeq (2\pi)^2 C(\vec{x}) \delta(t - r) \delta^{(2)}(\vec{p}_\perp),$$

where \vec{p}_\perp is the orthogonal component of \vec{p} to \vec{x} , and

$$C(\vec{x}) = \frac{\alpha_{EM}}{8\pi} (V_0 Z_{eff})^2 \frac{1}{r^2} \sin^2 \theta.$$

In the above, θ is the azimuthal angle of \vec{x} with respect to the z axis (see Fig.1). For $r \gg d$, we find

$$G^{(E)}(\vec{x}, \vec{p}; t) \simeq G^{(B)}(\vec{x}, \vec{p}; t),$$

and

$$G^{(E,B)}(\vec{x}, \vec{p}; t) \simeq G^{(E,B)}(\vec{x} + \vec{d}, \vec{p}; t) \simeq G^{(E,B)}(\vec{x} - \vec{d}, \vec{p}; t).$$

Then the Wigner function is finally expressed as

$$f_W(\vec{x}, \vec{p}; t) \simeq 4(2\pi)^2 C(\vec{x}) \left\{ 1 - \cos(\vec{p} \cdot \vec{d}) \right\} \delta(t - r) \times 2 \frac{1}{p^2} \delta^{(2)}(\Omega_{\vec{p}} - \Omega_{\vec{x}}), \quad (8)$$

where $\Omega_{\vec{p}}$ and $\Omega_{\vec{x}}$ are the solid angles for \vec{p} and \vec{x} , respectively. The factor 2 in the last term of the above equation comes from the two opposite directions contained in $\delta^{(2)}(\vec{p}_\perp)$. Equation (8) clearly shows that $f_W(\vec{x}, \vec{p}; t)$ is positive semi-definite.

From this Wigner function, the energy distributions in the \vec{x} and \vec{p} spaces are given by

$$\frac{d^3 \mathcal{E}}{d\vec{x}^3} = \frac{1}{(2\pi)^3} \int d^3 \vec{p} f_W(\vec{x}, \vec{p}; t), \quad (9)$$

and

$$\frac{d^3 \mathcal{E}}{d\vec{p}^3} = \frac{1}{(2\pi)^3} \int d^3 \vec{x} f_W(\vec{x}, \vec{p}; t), \quad (10)$$

respectively.

IV. PHOTON SPECTRUM

Substituting Eq. (8) into Eq. (10), we obtain the momentum spectrum. Because of the Dirac delta functions in Eq. (8), note that this is equivalent to the sum of all energies of the incoming photons to a detector at \vec{R}_D ,

$$\frac{d^3 \mathcal{E}}{d\vec{p}^3} = \frac{1}{(2\pi)^3} \int dt \int_{\vec{\Omega} \in D} d^2 \vec{\Omega}_{\vec{R}_D} R_D^2 f_W(\vec{R}_D, \vec{p}; t), \quad (11)$$

where the integral for the solid angle $\vec{\Omega}_{\vec{R}_D}$ is done within the domain D corresponding to the aperture of the detector. In the above, we integrate all photon energies coming into the detector. Reexpressing this with the photon number N , we have

$$\frac{d^3 N}{d\vec{p}_T^2 dy} = \frac{1}{2\pi^2} \frac{\alpha_{EM} (V_0 Z_{eff})^2}{p^2 \cosh^2 y} \left\{ 1 - \cos(2\vec{p} \cdot \vec{d}) \right\}, \quad (12)$$

where y represents the rapidity. See Appendix B. In the following calculations, we choose $V_0 = 1$.

For example, let us take $Z_{eff} \sim 80$ and $d \sim 1$ fm as a near central Au+Au collisions. In this case, the order of the magnitude of the photon spectrum is

$$\left. \frac{d^3 N(p)}{2\pi p_T dp_T dy} \right|_{y=0} \simeq 0.37 \times 10^{-3} \frac{Z_{eff}^2}{p_T^2} (1 - J_0(2p_T d)), \quad (13)$$

where J_n is the Bessel function of order n . In Fig. 2, we show the behavior of the above rough estimate (solid line) together with the PHENIX data, just for the sake of comparison. Although our calculation seems to be consistent with the experimental data, our idealization of full stopping is not well satisfied in RHIC energies. Rather, our model will be more suitable for the experiments of the lower energies such as NICA or FAIR program [27, 28] where the large stopping power is expected. Note that if we calculate the same spectrum assuming the incoherent radiations as is done in Ref. [20], the magnitude of the spectrum decreases by one or two order.

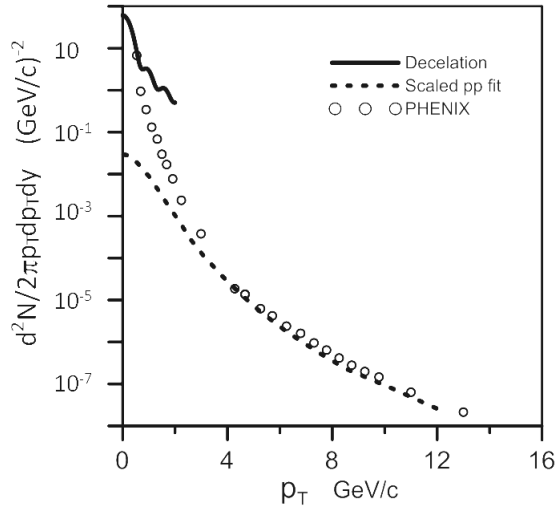


FIG. 2: The photon spectrum. The solid line represents the results from our model calculation. The circles and dashed line indicate the PHENIX data [21] and the scaled proton-proton collision fit, respectively.

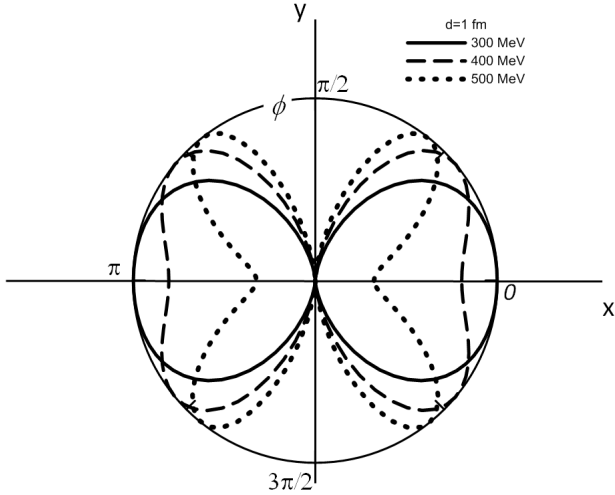


FIG. 3: The angular distributions at $y = 0$. The solid, dashed and dotted lines represent the results of $p_T = 300, 400$ and 500 MeV, respectively. The axes x and y correspond to those in Fig. 1.

The angular distribution of the photons reveals an interesting behavior as shown in Fig. 3. Here, we plotted only the factor $1 - \cos(2\vec{p} \cdot \vec{d})$ in the radial coordinate with respect to the azimuthal angle ϕ at the vanishing rapidity $y = 0$ where $p = p_T$, and we find that there are common dips at $\phi = \pm\pi/2$. These dips correspond to the direction of the normal vector to the reaction plane. If such a feature is measurable experimentally, we could determine the event plane unmistakably and even determine the parameter d quantitatively.

However, unfortunately, the total yield of such low energy photons is very small (< 20) even in a most favorable

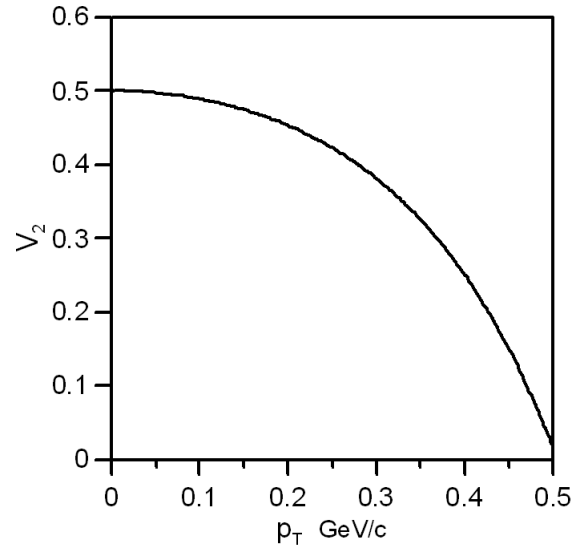


FIG. 4: Low energy behavior of v_2 of the direct photons obtained from the coherent radiations for $d = 1$ fm.

condition of our model. If we consider further experimental difficulties in the detection of the low energy photons, the determination of the event geometry in the EbyE base seems to be unrealistic.

On the other hand, the above peculiar behavior will be reflected in another tractable observables, the anisotropic parameter such as v_2 . In our model, v_2 is calculated as

$$v_2(p_T) = \frac{J_2(2p_T d)}{1 - J_0(2p_T d)}. \quad (14)$$

A similar expression was calculated by Ref. [29] in a different context. In Fig. 4, we plotted the above v_2 for $d = 1$ fm as before. In contrast to the well-known behavior of v_2 , the coherent electromagnetic radiations show an increasing v_2 for the lower p_T achieving its maximum value $1/2$ for $p_T \rightarrow 0$, independently of the value of d . Therefore, if such an increase of v_2 in the low energy photons ($p_T < 0.5$ GeV) is found experimentally, it can be considered as the genuine signal from the coherent electromagnetic radiations by the deceleration, although it will be affected by the incoherent radiations. See the discussion in Sec. V. Such a behavior is not expected from the usual hydrodynamic, kinetic or microscopic pictures of the collective flow mechanism [19, 30].

V. CONCLUDING REMARKS AND DISCUSSIONS

In this short exercise, we investigated the behavior of the low energy photons radiated by the deceleration processes of the two incident nuclei in relativistic heavy ion collisions. We assumed that the coherent radiations are dominant, so that the two colliding nuclei are replaced by point charges, and the deceleration mechanism is simply characterized by the Dirac delta function. We thus

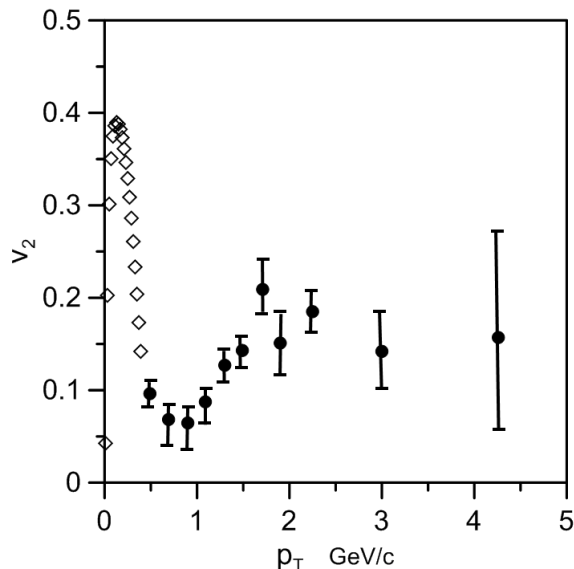


FIG. 5: v_2 from direct photons. Squares denote the results with the effects of incoherent mechanism given by Eq.(15) with $\Delta p = 0.2$ GeV, Filled circles indicate the experimental data from PHENIX[21].

consider the full stopping scenario like the Landau type initial condition, which may have better chance in lower energy heavy ion collisions such as coming NICA and FAIR experiments [27, 28].

We found that the angular distribution of the low energy photons reveals well the initial geometric configurations at the deceleration processes. Such a property is reflected in the anisotropic parameter v_2 , showing a very enhanced nature in the lower p_T . If the angular distribution is measurable in the EbyE basis, the initial geometry could be determined. However, the total photon multiplicity in our model is the order of $10 \sim 20$ in an optimistic situation, so that the EbyE basis analysis seems to be improbable. On the other hand, since these signals have characteristic patterns for a given initial geometry, they may be still useful to improve the determination of the initial condition by using, for example, the correlations with other particles. Another interesting possibility for the multiple soft photon emission mechanism was suggested in Ref.[31], but the nature of the angular distribution of the produced photons would be different from ours.

In this work, we considered a very idealized model of the deceleration where the coherent electromagnetic radiations occur from the overall nuclear charges, and did not discuss a mechanism to maintain such a coherence by rel-

ativistic heavy ion collisions. To clarify these points and examine the above possibilities, it is important to apply the present approach to more realistic initial conditions and possible collective deceleration mechanisms, for example, shock wave formation [11]. The Wigner function approach described here will be useful for this purpose. We leave this as a future task.

As shown in Fig. 4, our coherent radiations of the low energy photons exhibit an increasing v_2 as energy decreases, achieving its maximum value $1/2$ at $p_T = 0$. This is the case considering only the coherent radiations. As discussed, the coherence for higher momenta will be quickly destroyed and the incoherent photons should be dominant. We may roughly evaluate such an effect assuming that the coherent contribution vanishes exponentially with a characteristic scale Δp as a function of p_T , while the incoherent contribution becomes dominant for $p_T \gg \Delta p$. In such a case, the anisotropic parameter v_2 in Eq. (14) is replaced by

$$v_2(p_T) = \frac{J_2(2p_T d)}{1 + 2e^{2p_T/\Delta p}/Z_{eff} - J_0(2p_T d)}. \quad (15)$$

In Fig. 5, we show the results of Eq. (15) for $\Delta p = 0.2$ GeV with squares. For the sake of comparison, the PHENIX data are plotted together by filled circles [21]. Note that in the presence of the incoherent contribution, v_2 vanishes at $p_T = 0$ and the maximum is shifted to a finite value of p_T . Current experimental measurements of v_2 of the direct photons are only from 0.5 GeV and above [21], and thus it is still difficult to see whether the coherent radiation mechanism is present or not. However, it is interesting to note that the experimental data seems to show the beginning of such an increase for $p_T \leq 0.5$ GeV as is shown in Fig. 5, which is qualitatively in agreement with the behavior of v_2 calculated with the coherent radiation mechanism. Of course, our deceleration scenario is not applicable to the RHIC experiment, so that any direct comparison will not be appropriate. On the other hand, if this behavior of v_2 is attributed to the coherent radiations of the photons, we expect that such a signature should be enhanced in NICA and FAIR. In this aspect, the measurements of the lower energy direct photons are essential to clarify the presence of the coherent mechanism in relativistic heavy ion collisions.

The authors acknowledge E. L. Bratkovskaya, G. S. Denicol, M. Greif and C. Greiner for useful discussions and comments. We also thank E. Kokouline for calling our attention to Ref.[31]. This work is financially supported by CNPq and CAPES.

-
- [1] See, for example, R. Derradi de Souza, T. Koide and T. Kodama, Prog. Part. Nucl. Phys. **86**, 35 (2016).
 [2] J. Kapsta, Phys. Rev. C **15**, 1580 (1977).

- [3] J. D. Bjorken and L. McLerran, Phys. Rev. D **31**, 63 (1985).
 [4] J. Thiel et. al., Nucl. Phys. A **504**, 864 (1989).

- [5] V. Koch et. al., Phys. Lett. B**236**, 135 (1990).
- [6] T. Lippert et. al., Int. J. Mod. Phys. A**29**, 5249 (1991).
- [7] A. Dumitru et. al., Phys. Lett. B**318**, 583 (1993).
- [8] U. Eichmann and W. Greiner, J. Phys. G**23**, L65 (1997).
- [9] S. Jeon et. al., Phys. Rev. C**58**, 1666 (1998).
- [10] J. Kapusta and S. M. H. Wong, Phys. Rev. C**59**, 3317 (1999).
- [11] U. Eichmann et al., Phys. Rev. C**62** 044902 (2000).
- [12] P. A. Ruuskanen, Nucl. Phys. A**544**, 169c-182c (1992).
- [13] R. Chatterjee et al., Phys. Rev. C **83** 054908 (2011).
- [14] A. K. Chaudhuri and B. Sinha, Phys. Rev. C **83**, 034905 (2011).
- [15] C. Shen et. al., Phys. Rev. C**91**, 024908 (2015).
- [16] C. Gale et. al., Phys. Rev. Lett. **114**, 072301 (2015).
- [17] S. Endres et al., Phys. Rev. C**92**, 014911 (2015).
- [18] J. Alam, S. Raha and B. Sinha, Phys. Rep. **273** 243 (1996).
- [19] O. Linnyk, E. L. Bratkovskaya, W. Cassing, Prog. Part. Nucl. Phys. **87** 50 (2016).
- [20] T. S. Biró, M. Gyulassy and Z. Schram, Phys. Lett. B**708**, 276 (2012).
- [21] PHENIX collaboration, arXiv:1509.07758.
- [22] J. D. Jackson, *Classical Electrodynamics-3rd ed.* (Wiley, 1998).
- [23] L. Silberstein, Ann. d. Ohys. **22**, 579 (1907); **24**, 783 (1907);
- [24] H. Bateman, *The Mathematical Analysis of Electrical and Optical Wave Motion on the Basis of Maxwell's Equations* (Cambridge 1915, reprinted by Dover, New York, 1955).
- [25] I. Bialynicki-Birula, Act. Phys. Pol. A**86** 97 (1994).
- [26] P. Holland, Proc. R. Soc. A**461**, 359 (2005).
- [27] C. Höhne, J. Phys. Conf. Ser. **420**, 012016 (2013).
- [28] H. R. Schmidt, J. Phys. Conf. Ser. **509**, 012084 (2014).
- [29] T. S. Biró, M. Horváth, Zs. Schram, Eur. Phys. J. A**51** 75 (2015).
- [30] J.-F. Paquet, et al., arXiv:1509.06738.
- [31] P. Lichard and L. Van Hove, Phys. Lett. B**245** 605 (1999).
- [32] T. S. Biró, Z. Szendi and Z. Schram Euro. Phys. J. A**50** 62 (2014).

Appendix A: Sensitivity of rapidity distribution on deceleration

The trajectories (1) can be considered as if we take the vanishing τ_S limit of the parameterization of a continuous deceleration,

$$\vec{\xi}_1(t) = \begin{pmatrix} d \\ 0 \\ t V_0 \tanh\left(\frac{t}{\tau_S}\right) \theta(-t) \end{pmatrix}, \quad (\text{A1})$$

$$\vec{\xi}_2(t) = \begin{pmatrix} -d \\ 0 \\ -t V_0 \tanh\left(\frac{t}{\tau_S}\right) \theta(-t) \end{pmatrix}, \quad (\text{A2})$$

which is similar to Ref. [20], except for the difference in the argument of tanh.

Substituting this into the above calculations and taking the vanishing limit of τ_S , we find that the factor

$\{1 - \cos(2\vec{p} \cdot \vec{d})\}/p^2$ in Eq. (12) is replaced by

$$\frac{1}{2p^2} \left\{ \frac{1}{(1 - V_0 \tanh y)^2} + \frac{1}{(1 + V_0 \tanh y)^2} - 2 \frac{1}{1 - V_0^2 \tanh^2 y} \cos(2\vec{p} \cdot \vec{d}) \right\}. \quad (\text{A3})$$

In particular, in ultra-relativistic limit ($V_0 \rightarrow 1$), the angular distribution of the photons is given by

$$\frac{d^3 N}{d\vec{p}_T^2 dy} = \frac{1}{2\pi^2} \frac{\alpha_{EM} (V_0 Z_{eff})^2}{p^2} \left\{ \cosh(4y) - \cos(2\vec{p} \cdot \vec{d}) \right\}. \quad (\text{A4})$$

One can see that the rapidity distribution shows rather hyperbolic increase for $|y| \gg 1$, so that the photon yield is strongly enhanced in the forward and backward directions, while the angular distribution tends to be isotropic. However, for the central rapidity $y = 0$, the above result still coincides with Eq. (12). Therefore, in the plane at the central rapidity, the angular distribution of photons is independent of the deceleration mechanism as far as the time scale τ_S is small enough. This suggests a possibility that the behavior at $y = 0$ is relatively insensitive for deceleration mechanisms if the characteristic time scale of the deceleration is enough small.

For the sake of comparison, let us consider the incoherent limit. Then our spectrum for the deceleration of the Dirac delta function, Eq. (12), is replaced by

$$\frac{d^3 N}{d\vec{p}_T^2 dy} = \frac{1}{2\pi^2} \alpha_{EM} V_0^2 Z_{eff} \frac{1}{p^2 \cosh^2 y}. \quad (\text{A5})$$

On the other hand, in the small τ_S limit of the continuous deceleration, Eq. (A4), we have

$$\frac{d^3 N}{d\vec{p}_T^2 dy} = \frac{1}{2\pi^2} \alpha_{EM} V_0^2 Z_{eff} \frac{1}{p^2} \cosh(4y). \quad (\text{A6})$$

These rapidity dependences are, respectively, to be compared with the low energy limit and the Rindler acceleration cases discussed in Ref. [20]. However, in our case, Eq. (A5) does not necessarily correspond to the non-relativistic case, since V_0 can be arbitrary close to unity, and Eq. (A6) shows more quick increase in rapidity compared to the large deceleration limit of the Rindler case. That is, the difference of the deceleration mechanism changes drastically the rapidity distribution of photons. See also the related calculations in Ref. [32].

Appendix B: rapidity

Our variables shown in Fig. 1 can be expressed in term of the rapidity. For the sake of simplicity, we consider the case where the mass is negligibly small. Then the rapidity is defined by

$$y = \frac{1}{2} \ln \frac{p + p_z}{p - p_z}. \quad (\text{B1})$$

Then the energy and longitudinal momentum is expressed as

$$p = p_T \cosh y, \quad (\text{B2})$$

$$p_z = p_T \sinh y. \quad (\text{B3})$$

On the other hand, we can express p_z as

$$\cos \theta = \frac{p_z}{p}. \quad (\text{B4})$$

Substituting this into Eq. (B1), we have

$$\cos \theta = \tanh y, \quad (\text{B5})$$

$$\sin \theta = \frac{1}{\cosh y}. \quad (\text{B6})$$